

Search of Neutrino Magnetic Moments with a High-Purity Germanium Detector at the Kuo-Sheng Nuclear Power Station

H.T. Wong,^{1,*} H.B. Li,¹ S.T. Lin,^{1,2} F.S. Lee,¹ V. Singh,^{1,3} S.C. Wu,¹ C.Y. Chang,^{1,4} H.M. Chang,^{1,2} C.P. Chen,¹ M.H. Chou,¹ M. Deniz,^{1,5} J.M. Fang,⁶ C.H. Hu,⁷ H.X. Huang,⁸ G.C. Jon,¹ W.S. Kuo,⁷ W.P. Lai,¹ S.C. Lee,¹ J. Li,^{1,9,10} H.Y. Liao,^{1,2} F.K. Lin,¹ S.K. Lin,¹ J.Q. Lu,^{1,11} H.Y. Sheng,^{1,9} R.F. Su,⁶ W.S. Tong,⁷ B. Xin,^{1,8} T.R. Yeh,⁷ Q. Yue,¹⁰ Z.Y. Zhou,⁸ and B.A. Zhuang^{1,9}

(TEXONO Collaboration)

¹ *Institute of Physics, Academia Sinica, Taipei 115, Taiwan.*

² *Department of Physics, National Taiwan University, Taipei 106, Taiwan.*

³ *Department of Physics, Banaras Hindu University, Varanasi 221005, India.*

⁴ *Department of Physics, University of Maryland, College Park MD 20742, U.S.A.*

⁵ *Department of Physics, Middle East Technical University, Ankara 06531, Turkey.*

⁶ *Kuo-Sheng Nuclear Power Station, Taiwan Power Company, Kuo-Sheng 207, Taiwan.*

⁷ *Institute of Nuclear Energy Research, Lung-Tan 325, Taiwan.*

⁸ *Department of Nuclear Physics, Institute of Atomic Energy, Beijing 102413, China.*

⁹ *Institute of High Energy Physics, Chinese Academy of Science, Beijing 100039, China.*

¹⁰ *Department of Engineering Physics, Tsing Hua University, Beijing 100084, China.*

¹¹ *Department of Physics, Nanjing University, Nanjing 210093, China.*

(Dated: April 11, 2018)

A search of neutrino magnetic moments was carried out at the Kuo-Sheng Nuclear Power Station at a distance of 28 m from the 2.9 GW reactor core. With a high purity germanium detector of mass 1.06 kg surrounded by scintillating NaI(Tl) and CsI(Tl) crystals as anti-Compton detectors, a detection threshold of 5 keV and a background level of $1 \text{ kg}^{-1} \text{ keV}^{-1} \text{ day}^{-1}$ near threshold were achieved. Details of the reactor neutrino source, experimental hardware, background understanding and analysis methods are presented. Based on 570.7 and 127.8 days of Reactor ON and OFF data, respectively, at an average Reactor ON electron anti-neutrino flux of $6.4 \times 10^{12} \text{ cm}^{-2} \text{ s}^{-1}$, the limit on the neutrino magnetic moments of $\mu_{\bar{\nu}_e} < 7.4 \times 10^{-11} \mu_B$ at 90% confidence level was derived. Indirect bounds on the $\bar{\nu}_e$ radiative decay lifetimes were inferred.

PACS numbers: 14.60.Lm, 13.15.+g, 13.40.Em

I. INTRODUCTION

The strong evidence of neutrino oscillations from the solar, atmospheric as well as long baseline accelerator and reactor neutrino measurements implies finite neutrino masses and mixings [1, 2]. Their physical origin and experimental consequences are not fully understood. Experimental studies on the neutrino properties and interactions can shed light to these fundamental questions and provide constraints to the interpretations in the future precision oscillation experiments.

The couplings of neutrinos with the photons are generic consequences of finite neutrino masses, and are one of the important intrinsic neutrino properties [3] to explore. The neutrino electromagnetic vertex can be parametrized by terms corresponding to interactions without and with its spin, identified as the “neutrino charge radius” and “neutrino magnetic moments”, respectively.

This article reports on a search of the neutrino magnetic moments with reactor neutrinos at the Kuo-Sheng (KS) Nuclear Power Station in Taiwan. It extends over our previous publication [4] and covers the reactor neutrino spectra ($\phi(\bar{\nu}_e)$) and the other experimental features

in details. A factor of three larger data sample was used, and an analysis procedure combining information from all measured spectra was devised.

II. NEUTRINO MAGNETIC MOMENTS

An overview on the particle physics aspects of neutrino magnetic moments can be referred to a recent review [5] and the references therein. The neutrino magnetic moment (μ_ν) is an experimentally observable parameter which characterizes a possible coupling between neutrino mass eigenstates ν_i and ν_j with the photon whereby the helicity-state is flipped:

$$(\nu_i)_L \rightarrow \gamma \rightarrow (\nu_j)_R \quad (1)$$

as depicted schematically in Figure 1. The vertex marked “?” denotes the unknown physics to be explored. The parameter μ_ν is usually expressed in units of the Bohr magneton:

$$\mu_B = \frac{e}{2m_e} \quad ; \quad e^2 = 4\pi\alpha_{em} \quad , \quad (2)$$

where α_{em} is the fine-structure constant and m_e is the electron mass. Both *diagonal* and *transition* moments

are possible, corresponding to the cases where $i = j$ and $i \neq j$, respectively. Symmetry principles place constraints on the possible channels [6] and require that the diagonal moments vanish for Majorana neutrinos. The study of neutrino magnetic moments is, in principle, a way to distinguish between Dirac and Majorana neutrinos – a crucial unresolved issue in neutrino physics. For example, if a finite μ_ν is observed in the laboratory, and electron anti-neutrinos ($\bar{\nu}_e$) from the Sun is detected with a spectrum consistent with the oscillation and solar model parameters, neutrinos would be Majorana particles. Recent derivations [7] of model-independent μ_ν -ranges indicated that upper bounds for Dirac neutrinos are several orders of magnitude more stringent than the current experimental limits. Consequently, observations of μ_ν at the present sensitivities will imply that neutrinos are Majorana.

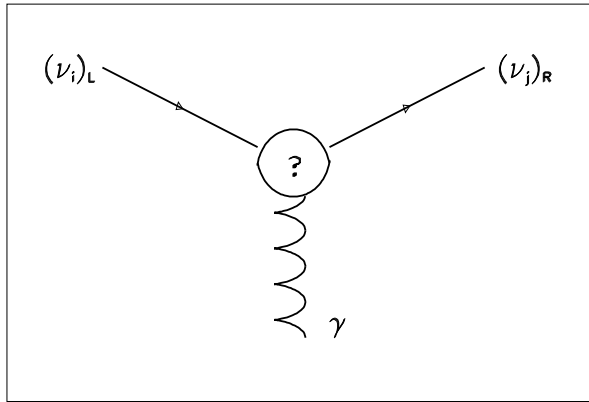


FIG. 1: The schematic diagram of the neutrino-photon interaction vertex which involves a change of the helicity-states. The coupling is parametrized by the neutrino magnetic moment.

Once a model is specified, the vertex “?” is known and μ_ν can be calculated from first principles. Minimally-Extended Standard Model with massive Dirac neutrinos [8] gives $\mu_\nu \sim 10^{-19} [m_\nu/1 \text{ eV}] \mu_B$ which is far too small to have any observable consequences. Incorporation of additional physics, such as Majorana neutrino transition moments or right-handed weak currents, can significantly enhance μ_ν to the experimentally relevant ranges [9]. Supersymmetry as well as extra-dimensions [10] can also contribute to the process.

The parameter μ_ν for neutrinos with energy E_ν produced as ν_i at the source and after traversing a distance L is given by [11]

$$\mu_\nu^2(\nu_i, L, E_\nu) = \sum_j \left| \sum_i U_{ji} e^{-iE_\nu L} \mu_{ij} \right|^2, \quad (3)$$

where U_{li} is the neutrino mixing matrix and μ_{ij} are the coupling constants between ν_i and ν_j with the photon. Consequently, μ_ν is therefore an effective and convoluted

parameter and the interpretations of experimental results depend on the exact ν_l compositions at the detectors. In this paper, we write $\mu_{\bar{\nu}_e} = \kappa_e \times 10^{-10} \mu_B$ and work with the parameter κ_e for simplicity.

The neutrino spin-flavor precession (SFP) mechanism [12], with or without matter resonance effects in the solar medium, has been used to explain solar neutrino deficit [13]. This scenario is compatible with all solar neutrino data. The terrestrial KamLAND experiment, however, recently confirmed the Large Mixing Angle (LMA) parameter space of the matter oscillation scenario as *the* solution for the solar neutrino problem [14], such that SFP can be excluded as the dominant contribution in solar neutrino physics [15]. Alternatively, the measured solar neutrino ν_\odot -e spectral shape has been used to set limit of $\kappa_\odot < 1.1$ at 90% confidence level (CL) for the “effective” ν_\odot magnetic moment [11, 16] which is different from that of a pure $\bar{\nu}_e$ state derived in reactor experiments. Other astrophysical bounds on μ_ν were mostly derived from the consequences from a change of the neutrino spin-states in the astrophysical medium [5, 17], typically of the range $\kappa_{\text{astro}} < 10^{-2} - 10^{-3}$. However, these bounds are model-dependent and involve implicit assumptions on the neutrino properties.

Direct laboratory experiments [5] on μ_ν utilize accelerator and reactor neutrinos as sources, and are conducted under controlled conditions. The most sensitive searches are usually performed by experiments studying neutrino-electron scatterings [18]:

$$\nu_l + e^- \rightarrow \nu_x + e^-. \quad (4)$$

The experimental observable is the kinetic energy of the recoil electrons (T). A finite μ_ν will contribute to a differential cross-section term given by:

$$\left(\frac{d\sigma}{dT} \right)_{\mu_\nu} = \frac{\pi \alpha_{em}^2 \mu_\nu^2}{m_e^2} \left[\frac{1 - T/E_\nu}{T} \right]. \quad (5)$$

The signature is an excess of events over those due to Standard Model of electroweak interactions (SM) and other background processes, which exhibit the characteristic $1/T$ spectral dependence. Limits from negative searches are valid for both Dirac and Majorana neutrinos and for both diagonal and transitional moments.

The neutrino radiative decay [19] for the process

$$\nu_i \rightarrow \nu_j + \gamma \quad (6)$$

is another manifestation of the neutrino electromagnetic couplings where a change of the neutrino helicity-states takes place. A final-state real photon is produced in the process, unlike the μ_ν -effects on neutrino-electron scatterings, where only virtual photons are involved. The decay rate Γ_{ij} and the decay lifetime τ_{ij} is related to μ_{ij} via [20]

$$\Gamma_{ij} = \frac{1}{\tau_{ij}} = \frac{1}{8\pi} \frac{(m_i^2 - m_j^2)^3}{m_i^3} \mu_{ij}^2, \quad (7)$$

where $m_{i,j}$ are the masses for $\nu_{i,j}$.

III. DIRECT SEARCHES WITH REACTOR NEUTRINOS

Reactor neutrinos provide a sensitive probe for laboratory searches of $\mu_{\bar{\nu}_e}$, taking advantages of the high $\bar{\nu}_e$ flux, low E_ν and better experimental control via the reactor ON/OFF comparison. The measurable electron recoil energy spectra due to SM and μ_ν (at $\kappa_e=1.0$) scatterings with reactor- $\bar{\nu}_e$'s, denoted respectively by $\Phi_e(SM)$ and $\Phi_e(\mu_\nu)$, are displayed in Figure 2. A finite $\mu_{\bar{\nu}_e}$ would manifest itself as excess of events in the ON spectra over the background as derived from the OFF data, which have a $1/T$ energy spectrum.

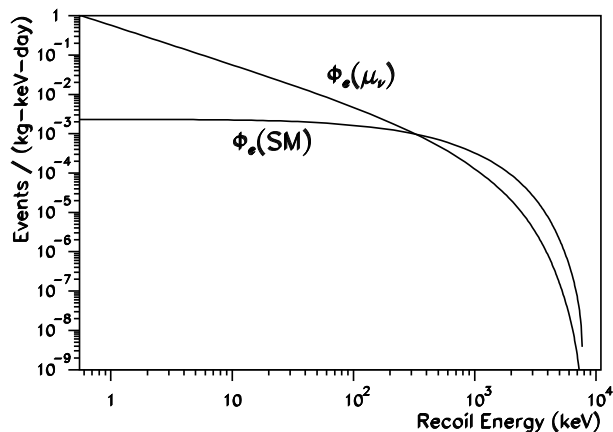


FIG. 2: The expected recoil spectra due to neutrino-electron scattering with reactor $\bar{\nu}_e$ at a flux of $10^{13} \text{ cm}^{-2}\text{s}^{-1}$. Contributions from Standard Model [$\Phi_e(SM)$] and magnetic moments [$\Phi_e(\mu_\nu)$] at $10^{-10} \mu_B$ are shown.

Neutrino-electron scatterings were first observed in the pioneering experiment [21] at Savannah River where plastic scintillators were adopted as target surrounded by NaI(Tl) crystal scintillators as anti-coincidence counters. A revised analysis of the data by Ref [18] with improved input parameters gave a positive signature consistent with the interpretation of a finite $\mu_{\bar{\nu}_e}$ at $\kappa_e=2-4$. An intrinsic error source of this experiment was the use of a proton-rich target. The cross-section for the proton-capture reaction:

$$\bar{\nu}_e + p \rightarrow e^+ + n \quad (8)$$

is much larger than that for $\bar{\nu}_e$ -e scatterings. Other results came from the Kurtchatov [22] and Rovno [23] experiments which quoted limits of $\kappa_e < 2.4$ and < 1.9 at 90% CL, respectively. A recent experiment MUNU [24] at the Bugey reactor adopted a time projection chamber with CF_4 gas surrounded by active liquid scintillator as anti-Compton vetos. A limit of $\kappa_e < 0.9$ at 90% CL

was set with 66.6 days of data at a threshold of 700 keV. The lowest-energy bin was at a $\sim 2\sigma$ excess over the SM value.

A global analysis was performed [25] which combined simultaneously the μ_ν data from the reactor and solar neutrino experiments, as well as the LMA oscillation parameters constrained by solar neutrino and KamLAND results. Only Majorana neutrinos were considered such that there were only transition moments. A “total” magnetic moment vector $\Lambda=(\mu_{23}, \mu_{31}, \mu_{12})$ was defined, such that its amplitude was given by $|\Lambda|^2 = \frac{1}{2} \text{Tr}(\mu^+ \mu)$. A global fit produced 90% CL limits of $|\Lambda| < 4.0 \times 10^{-10} \mu_B$ from solar and KamLAND data only, while $|\Lambda| < 1.8 \times 10^{-10} \mu_B$ when reactor data were added. The results indicate the important role of reactor experiments in constraining the magnetic moment effects.

The systematic effects related to the poorly-known neutrino spectra were difficult to control in the 1 MeV range relevant to the previous experiments [26]. The approach of the KS experiment is to achieve a threshold of ~ 10 keV range through a matured and reliable detector technology – high-purity germanium (HPGe) detector. Three important advantages can be realized which significantly enhance the sensitivities and robustness of the results: (1) the potential signal rate is much increased due to the $1/T$ energy dependence of Eq. 5; (2) as shown in Figure 2, the event rates from $\Phi_e(\mu_\nu)$ are 24 times those of $\Phi_e(SM)$ at $T \sim 10$ keV and $\kappa_e \sim 1$, such that the uncertainties in the SM background do not affect the μ_ν signals; (3) Eq. 5 is mostly independent of E_ν at ~ 10 -100 keV, such that the μ_ν signals depends only on the well-known total reactor neutrino flux but *not* the details of $\phi(\bar{\nu}_e)$, thereby reducing the systematic uncertainties. In contrast, the poorly-modeled $\phi(\bar{\nu}_e)$ at ~ 1 MeV gives rise to uncertainties in the irreducible $\Phi_e(SM)$ background (which is 2.7 times the $\Phi_e(\mu_\nu)$ -signals at $\kappa_e \sim 1$) for experiments operating at this energy range.

We report in this article data taken at KS with HPGe. There are three Reactor ON/OFF data taking periods, the key information of which are summarized in Table I.

IV. REACTOR NEUTRINO SPECTRUM

The $\bar{\nu}_e$'s emitted in power reactors are predominantly produced through β -decays of (a) the fission products, following the fission of the four dominant fissile isotopes: ^{235}U , ^{238}U , ^{239}Pu and ^{241}Pu , and (b) ^{239}U , following the neutron capture on the ^{238}U fuel: $^{238}\text{U}(n,\gamma)^{239}\text{U}$.

The KS neutrino laboratory, as depicted schematically in Figure 3, is located at a distance of 28 m from Core #1 of the Kuo-Sheng Nuclear Power Station in Taiwan. The nominal thermal power output is 2.9 GW. The standard operation includes about 18 months of Reactor ON time at nominal power followed by about 50 days of Reactor outage OFF period when about a third of the fuel

TABLE I: Summary of the key information on the three data taking periods.

Period	Data Taking Calendar Time	Reactor ON Real Time (days)	Reactor ON Live Time (days)	Reactor OFF Real Time (days)	Reactor OFF Live Time (days)	DAQ Live Time (%)	Average $\bar{\nu}_e$ flux ($10^{12} \text{ cm}^{-2} \text{ s}^{-1}$)
I	July 2001 - April 2002	188.2	180.1	55.1	52.7	95.7	6.29
II	Sept. 2002 - April 2003	125.8	111.7	34.4	31.5	89.4	6.53
III	Sept. 2004 - Oct. 2005	303.9	278.9	48.7	43.6	91.5	6.51
Total	—	617.9	570.7	138.2	127.8	92.4	6.44

TABLE II: Fractional mass compositions, relative fission contributions and neutrino yield per fission for the four fissile isotopes and the ^{238}U neutron capture. All values are time-dependent and only typical levels are given.

Channels	Fractional Compositions by Mass (%)	Relative Rates per Fission	Neutrino Yield per Event	Neutrino Yield per Fission
^{235}U Fission	1.5	0.55	6.14	3.4
^{238}U Fission	98.0	0.07	7.08	0.5
^{239}Pu Fission	0.4	0.32	5.58	1.8
^{241}Pu Fission	<0.1	0.06	6.42	0.4
^{238}U (n, γ) ^{239}U	—	0.60	2.00	1.2
Total	—	—	—	7.3

Kuo-Sheng Nuclear Power Station : Reactor Building

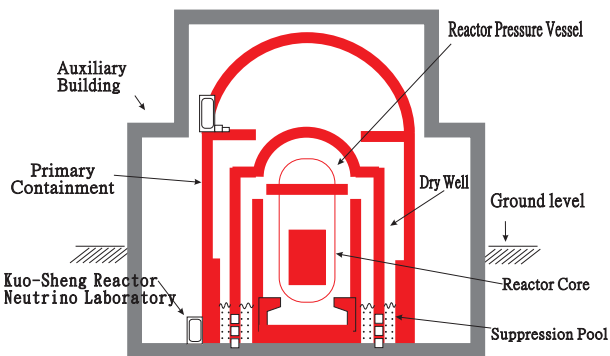


FIG. 3: Schematic layout of the Kuo-Sheng Neutrino Laboratory in relation to the core of the power reactor.

elements are replaced. Reactor operation data on the thermal power output and control rod status as functions of time and locations within the core were provided to the experiment by the Power Station. A set of software programs [27] was specifically developed, in association with the commercial SIMULATE-3 and CASMO-3 codes [28], both of which are extensively used in the field of nuclear reactor core analyses. The variations of the thermal power output, as well as the fission rates and $\bar{\nu}_e$ -flux of the fissile isotopes during Period-III are displayed in Figures 4a-c. At steady state operation, the total fission rates and the total neutrino fluxes were constant to better than 0.1% and 0.2%, respectively. Data taken during the short durations of unscheduled reactor stops were included into the Reactor-OFF category.

The typical $\bar{\nu}_e$ -yield for these channels, as well as their

relative contributions per fission are summarized in Table II. The $\bar{\nu}_e$ -yields for the fission elements were adopted from Ref. [29], following a survey of the fission daughter isotopes and the subsequent β -decays necessary to reach stability. The ^{238}U neutron capture rate of 0.6 per fission were evaluated by two independent methods: (a) via full neutron transport calculations of the neutrons in the reactor core [30, 31], and (b) by evaluating the difference in the decrease of the amount of ^{238}U and the ^{238}U fission rate. Results derived by both methods were consistent to a few percent.

The $\phi(\bar{\nu}_e)$'s of the five channels, as depicted in Figure 5a, were adopted from Ref. [18] for the fission $\bar{\nu}_e$'s, while those following ^{238}U neutron capture were derived from standard β -spectra of ^{239}U and ^{240}Np . The components were summed according to the relative contributions per fission, and the resulting total $\phi(\bar{\nu}_e)$ is shown in Figure 5b. This spectrum was used as input in deriving the expected electron recoil spectra in Figure 2. The evaluated $\bar{\nu}_e$ -fluxes for the three periods are given in Table I, where the weighted average is $6.4 \times 10^{12} \text{ cm}^{-2} \text{ s}^{-1}$.

The modeling of $\phi(\bar{\nu}_e)$ above the threshold of the reaction of Eq. 8 from reactor operation data has been well-established. Accuracies of better than 1.4% and 5% between calculations and measurements were achieved in the integrated [32] and differential [33] spectra. The evaluation of $\phi(\bar{\nu}_e)$ at energy below 2 MeV, on the other hand, is much more complicated [26]. Many input parameters remain unknown and there are no measurements to cross-check. Consequently, the $\Phi_e(SM)$ recoil spectra below the MeV range in Figure 2 were subjected to large uncertainties. However, the spectra $\Phi_e(\mu_\nu)$ at 10-100 keV were accurately predicted due to the E_ν -independence of

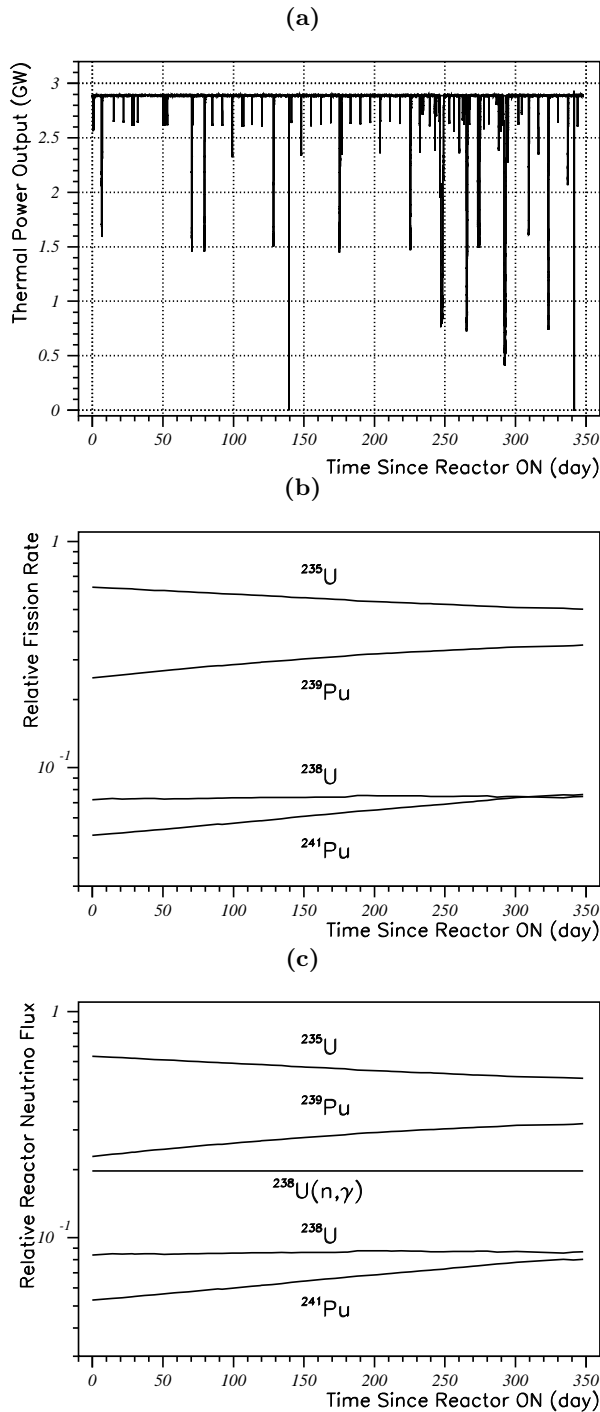


FIG. 4: The variations of the (a) thermal power output, as well as the (b) relative fission rates and (c) $\bar{\nu}_e$ -flux of the fissile isotopes over Period-III of data taking. The reactor outage OFF period was completed on Day-0.

Eq. 5. They followed a $1/T$ profile and depended only on the total $\bar{\nu}_e$ -fluxes of Table I, which were calculated with an expected accuracy of a few percent.

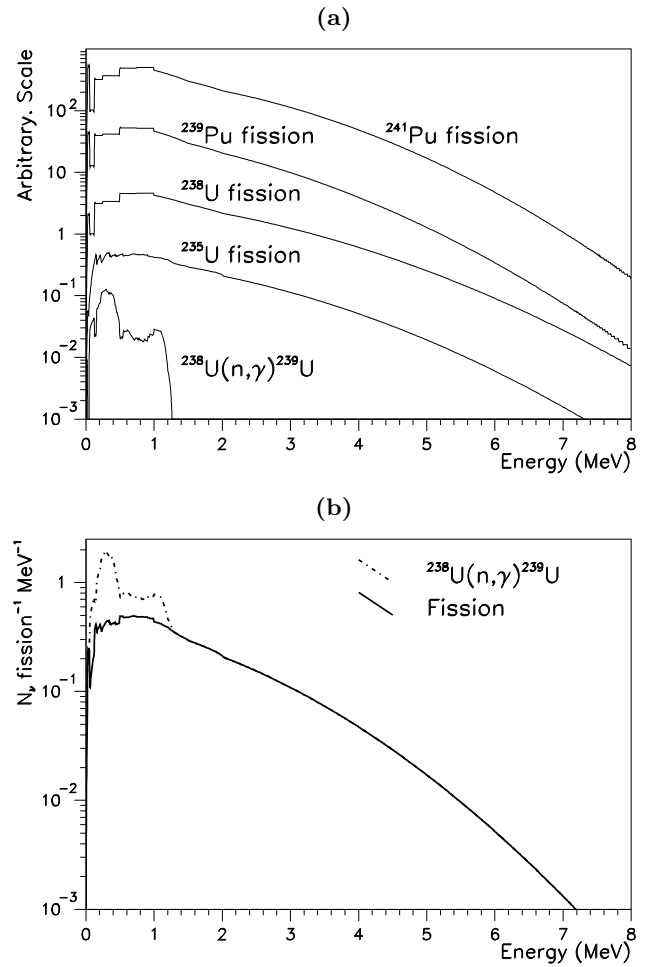


FIG. 5: (a) Spectral shape for reactor neutrinos due to individual production channels. (b) Total spectrum at the typical power reactor operation.

V. EXPERIMENTAL SET-UP

A research program on low energy neutrino physics [34] is being pursued by the TEXONO Collaboration at the KS Neutrino Laboratory. The laboratory is equipped with an outer 50-ton shielding structure depicted schematically in Figure 6, consisting of, from outside in, 2.5 cm thick plastic scintillator panels with photo-multiplier tubes (PMTs) readout for cosmic-ray veto (CRV), 15 cm of lead, 5 cm of stainless steel support structures, 25 cm of boron-loaded polyethylene and 5 cm of OFHC copper. The innermost volume with a dimension of $100 \times 80 \times 75 \text{ cm}^3$ provides the flexibilities of placing different detectors for different physics topics. During the I-III data taking periods listed in Table I, both the HPGc and a CsI(Tl) scintillating crystal array [35] together with their associated inner shieldings were placed in the inner volume. The CsI(Tl) array is for the measurement of neutrino-electron scattering cross-sections. The μ_ν -search reported in this article was performed with

the HPGe detector.

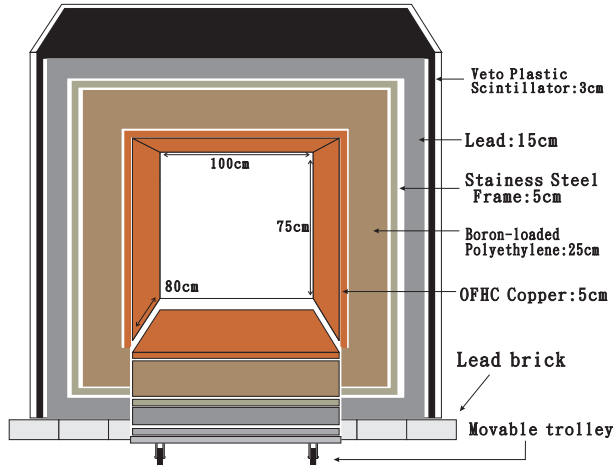


FIG. 6: The shielding design of the KS Neutrino Laboratory. Detectors and inner shieldings were placed in the inner target volume.

As indicated in Figure 3, the laboratory is located at the ground floor of the reactor building at a depth of 12 m below sea-level and with about 25 m water equivalence of overburden. The primary cosmic-ray hadronic components are eliminated while the muon flux is reduced by a factor of 4. Ambient γ -background at the reactor site is about 10 times higher in the MeV range than that of a typical laboratory, dominated by activity due to ^{60}Co and ^{54}Mn (half-lives 5.27 years and 312 days, respectively) present as dust in the environment. Both isotopes are produced by neutron activation on the construction materials at the reactor core. The dust can get settled on exposed surfaces within hours and is difficult to remove. Some earlier prototype detectors were contaminated by such. Attempts to clean the surfaces in situ resulted in higher contaminations. Accordingly, the various detector and inner shielding components were carefully washed and wrapped by several layers of plastic sheets before transportation to KS. Outer layers were removed in situ only prior to installation, while inner layers were replaced between data taking periods. Neutron background is comparable to that of a typical surface location, with no observable differences between the ON and OFF periods.

The HPGe set-up is shown schematically in Figure 7. It is a coaxial germanium detector [37] with an active target mass of 1.06 kg. The construction materials and detector geometry followed the “Ultra Low Background (ULB)” standards. The lithium-diffused outer electrode is 0.7 mm thick. The end-cap cryostat, also 0.7 mm thick, is made of OFHC copper. Both of these features provide total suppression to ambient γ -background below 60 keV, such that events below this energy are either due to internal activity or ambient MeV-range γ 's via Compton scattering. Consequently, the background profile should

be smooth and continuous below 60 keV down to the ranges where atomic effects are important. The HPGe was surrounded by an anti-Compton veto (ACV) detector system made up of three components: (1) an NaI(Tl) “well-detector” of thickness 5 cm that fit onto the end-cap cryostat and is coupled to a 12 cm PMT readout through an additional 7 cm of CsI(Tl) as active light guide; (2) an NaI(Tl) “ring-detector” of thickness 5 cm at the joint of the cryostat; and (3) a 4 cm thick CsI(Tl) “base-detector” at the bottom. All of these ACV detectors were assembled within mechanical structures made of OFHC copper, and were read out by PMTs with low-activity glass. The assembly was further surrounded by 3.7 cm of OFHC copper inner shielding. Another OFHC copper wall of thickness 10 cm provided additional shieldings on the side of the liquid nitrogen dewar and pre-amplifier electronics. The inner shieldings and detectors were covered by a plastic bag connected to the exhaust line of the dewar, serving as a purge for the radioactive radon gas.

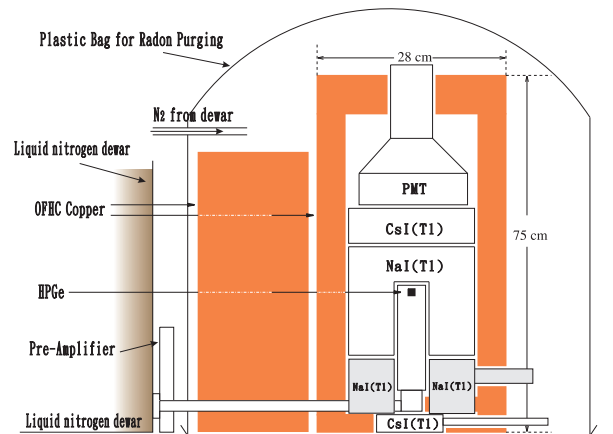


FIG. 7: Schematic layout of the HPGe with its anti-Compton detectors as well as inner shieldings and radon purge system.

The electronics and data acquisition (DAQ) system [36] of the HPGe detector assembly is illustrated schematically in Figure 8. The HPGe pre-amplifier signals were distributed to two spectroscopy amplifiers at the same 4 μs shaping time but with different gain factors. The amplifier signals were fed to a discriminator with a minimal threshold. The discriminator output provided the on-line triggers, ensuring all the events down to the electronics noise edge of 5 keV were recorded. The amplifier output of the HPGe and the PMT signals from the ACV detectors were recorded by 20 MHz Flash Analog to Digital Converter (FADC) modules with 8-bit dynamic range for a duration of 10 μs and 25 μs before and after the trigger, respectively. The discriminator output for the various channels of all three systems (HPGe, ACV, CRV), as well as the timing output of the CRV PMTs, were also recorded. The redundancy of the read-out channels enhanced robustness and stability to the

detector performance. A random trigger (RT) was generated by an external clock at a sampling rate of 0.1 Hz. The RT events provided accurate measurements of the pedestal levels, the DAQ dead time as well as the various efficiency factors. The data were read out via the VME bus through an VME-PCI interface [38] to a PC running on Linux operating system. The data were saved on hard disks. The DAQ system remained active for 2 ms after a trigger to record possible time-correlated signatures. The typical data taking rate for the HPGe sub-system was about 1 Hz. The DAQ dead time was about 4 ms and 2 ms per event for the HPGe and CsI(Tl) triggers, respectively. The system live times are listed in Table I. They varied among the three periods because of the different trigger rates.

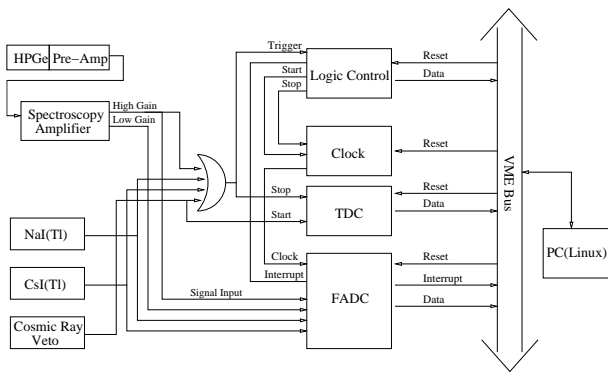


FIG. 8: Schematic layout of the electronics and data acquisition systems of the HPGe and the associated ACV and CRV detectors.

The KS Laboratory is connected with the control center at Academia Sinica (AS) through the telephone lines via MODEM. Internet connections are prohibited due to security reasons. During steady-state data taking, the experiment operated automatically without the necessity of human presence. The operating conditions were constantly monitored via the MODEM. Stability of key parameters like temperatures, liquid nitrogen levels, trigger rates and DAQ live times were checked. The KS Nuclear Power Station can be reached by an hour’s drive from AS. The laboratory was visited typically once a week, when manual checks and calibrations were performed. Hard disks were retrieved and brought back to AS where data were archived and copied. A total of ~ 125 Gbytes of raw data were recorded in the three data taking periods by the HPGe system. The data to be processed were installed on to an external disk array storage system [39] with 1.6 Tbytes total storage capacity. Relevant and high-level data on physical quantities were then extracted and distributed among the users, on which data analysis were performed.

VI. DATA ANALYSIS AND UNDERSTANDING

Scatterings of $\bar{\nu}_e$ -e inside the Ge target would manifest as “lone-events” uncorrelated with other detector systems. These events were extracted from the raw data through selection criteria including pulse shape analysis (PSA), anti-Compton (ACV) and cosmic-ray vetos (CRV).

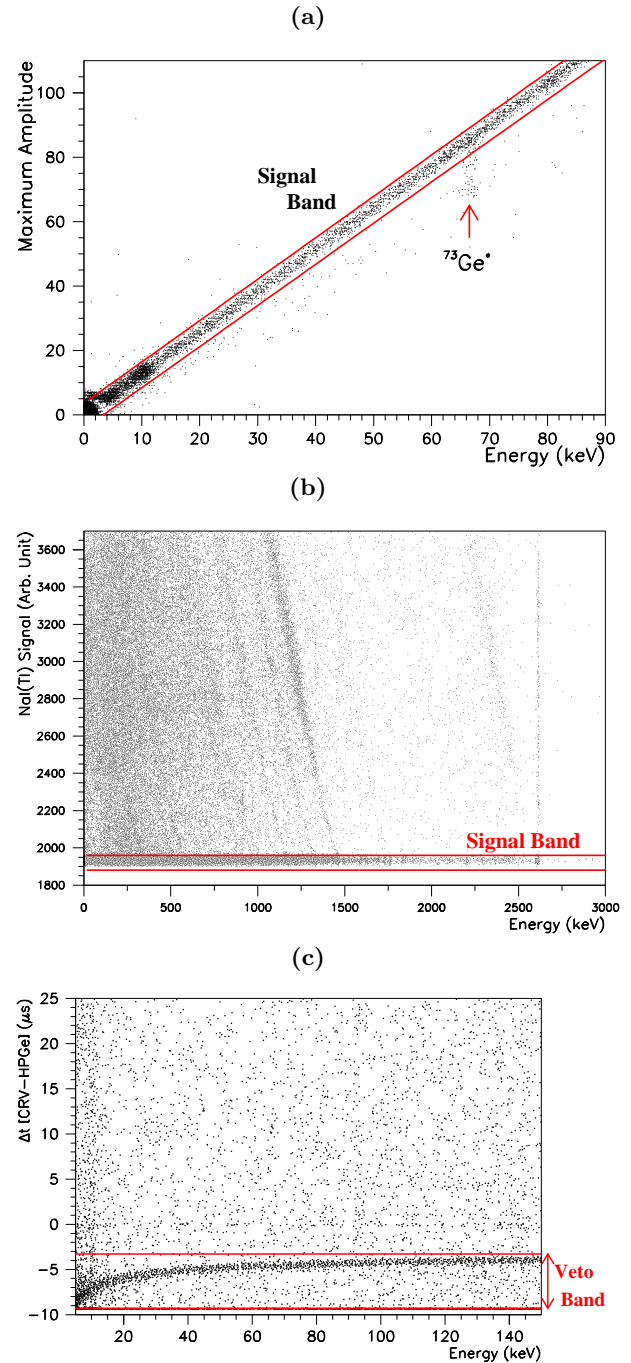


FIG. 9: Selection procedures of the recorded data : (a) pulse shape analysis, (b) anti-Compton selection, and (c) cosmic-ray veto.

As displayed in the correlation plot between pulse area and amplitude in Figure 9a, spurious background due to accidental and delayed “cascade” events were suppressed by PSA. In particular, the structure at 66 keV was from the decays of $^{73}\text{Ge}^*$ via the emissions of two photons separated by a half-life of 4.6 μs . The ACV and CRV cuts suppressed Compton scattering and cosmic-ray induced events, respectively. The scattered plot of HPGe and NaI(Tl) well-detector events is shown in Figure 9b. A software threshold of about 5 keV was adopted for the ACV detector to define the veto regions. The various slanted bands were due to full energy depositions of γ -rays in the two detectors, such as those from ^{40}K and the ^{238}U and ^{232}Th series. The vertical band at 2614 keV originated from the coincidence of the γ -ray cascade following the decays of ^{208}Tl . The timing correlations between CRV and HPGe events are shown in Figure 9c. The PMT pulses from the CRV were fast (10 ns rise time) and therefore arrived before the HPGe signals which were processed through amplifiers with 4 μs shaping time. The time difference increased with lower energy because the trigger timing was defined by a constant-threshold discriminator. The selected regions for the lone-events are displayed in the respective plots in Figure 9.

The background suppression factors as well as the signal survival efficiencies for the three data taking periods are summarized in Table III. The RT events were uncorrelated to the other parts of the detector systems – similar to the neutrino-induced events. The survival probabilities of the RT events along the various stages of the analysis procedures provided accurate measurements of the DAQ and analysis efficiencies. The DAQ live time is the ratio between RT events actually recorded on disk to the total numbers of RT signals generated by the clock. The ACV and CRV selection efficiencies are the fractions of the RT events which survived the cuts. Only loose cuts of $\pm 5\sigma$ around the signal band were used in the PSA cut as shown in Figure 9a, such that its efficiency is close to unity.

As illustrations, the measured spectra in Period-III before and after the ACV+CRV cuts for the Reactor ON data are depicted in Figure 10. The spectra after the event selection criteria, also for Period-III, are displayed in Figures 11a and 11b for the high and low energy ranges, respectively. The main γ -lines were identified and tabulated in Table IV. Most of the γ -activities were due to natural background from the ^{238}U and ^{232}Th series, as well as from ^{40}K and ^{235}U . The existence of activities from ^{235}U is particularly instructive. The low-energy lines implies that the source should be close to the target, most probably inside the OFHC cryostat, where ^{238}U and ^{232}Th should also be present in larger amount. These activities were likely to originate from the front-end pre-amplifier components located in the vicinity of the HPGe target. These were expected to be one of the important background sources.

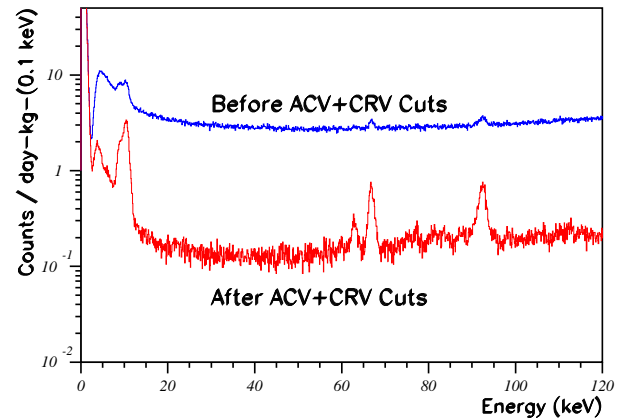


FIG. 10: Measured spectra before and after the ACV+CRV cuts for the Reactor ON data in Period-III.

Besides natural radioactivity, there were evidence of ^{60}Co and ^{54}Mn , both being known contaminations within the reactor building. Decay profiles were observed for ^{54}Mn consistent with its nominal decay life-time. The peak at 662 keV was due to ^{137}Cs activity in the CsI(Tl) ACV detector located near the HPGe. There was an unidentified line at 249.8 keV. The intensity was uniform to $<4\%$ in both ON and OFF periods but the short-duration rates fluctuated more than the statistical uncertainties would allow. No interpretations consistent with the other spectral features could be found.

The various γ -lines also provided in situ energy calibration as well as independent measurements and consistency checks to the stability and efficiency factors complementary to the RT events. Details on background and detector stabilities will be presented in Section VII in connection with the discussions on the systematic uncertainties.

The low energy spectrum of Figure 11b is relevant to the studies of neutrino magnetic moments. A detector threshold of 5 keV and a background of $\sim 1 \text{ keV}^{-1}\text{kg}^{-1}\text{day}^{-1}$ above 12 keV were achieved. The background level is comparable to the typical range in underground Cold Dark Matter experiments. This is a notable achievement for an experiment at shallow-depth – and in the vicinity of a power reactor core. Several γ -lines can be identified: (a) Ga X-rays at 10.37 keV and $^{73}\text{Ge}^*$ at 66.7 keV from internal cosmic-induced activities, (b) ^{234}Th at 63.3 keV and 92.6 keV from the ^{238}U series due to residual ambient radioactivity close to the target, and (c) a line at 80.9 keV in the OFF spectrum, to be examined in a subsequent paragraph. The copper cryostat as well as the inactive surface electrode of the HPGe provided total suppression to external low energy photons. Consequently, the measured spectra did not exhibit any structures above the the Ga X-rays end point at 12 keV up to about 60 keV.

Time variations of two features were observed in the

TABLE III: Summary of the event selection procedures as well as their background suppression and signal efficiency factors. The survival probabilities are defined as the ratio between the events selected to those prior to these cuts but after previous cuts were applied.

Event Selection	Background Suppression			Signal Efficiency		
	I	II	III	I	II	III
Raw Data	1.0	1.0	1.0	1.0	1.0	1.0
Pulse Shape Analysis (PSA)	>0.99	>0.99	>0.99	>0.99	>0.99	>0.99
Anti-Compton Veto (ACV)	0.054	0.051	0.058	0.99	0.99	0.99
Cosmic-Ray Veto (CRV)	0.92	0.85	0.80	0.95	0.94	0.93
Combined Efficiency	0.050	0.043	0.046	0.95	0.93	0.92

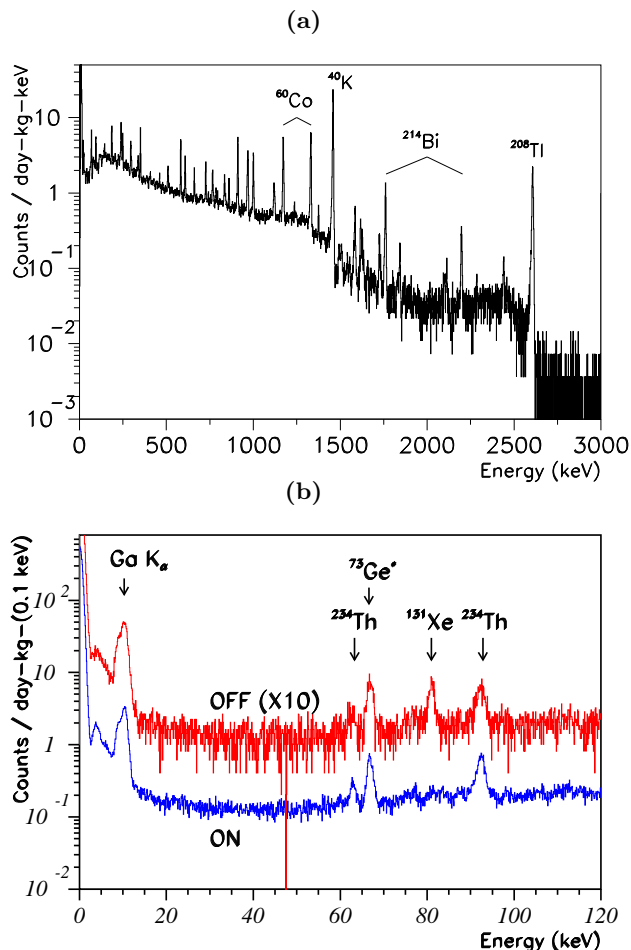


FIG. 11: Measured spectra in Period-III after all the selection criteria were applied for: (a) the full energy range and (b) the range below 120 keV relevant to magnetic moment studies. Key γ -lines were identified. Both Reactor ON and OFF spectra are separately displayed in (b).

low energy spectrum displayed in Figure 11b. The intensity of the 10.37 keV Ga X-ray peak decayed with time, as illustrated in Figure 12a in the case of data from Period-III. The best-fit half-lives of 275 ± 14 days and 9.6 ± 3.0 days to a double-exponential function agree well with the decays of ^{68}Ge and ^{71}Ge both of which were

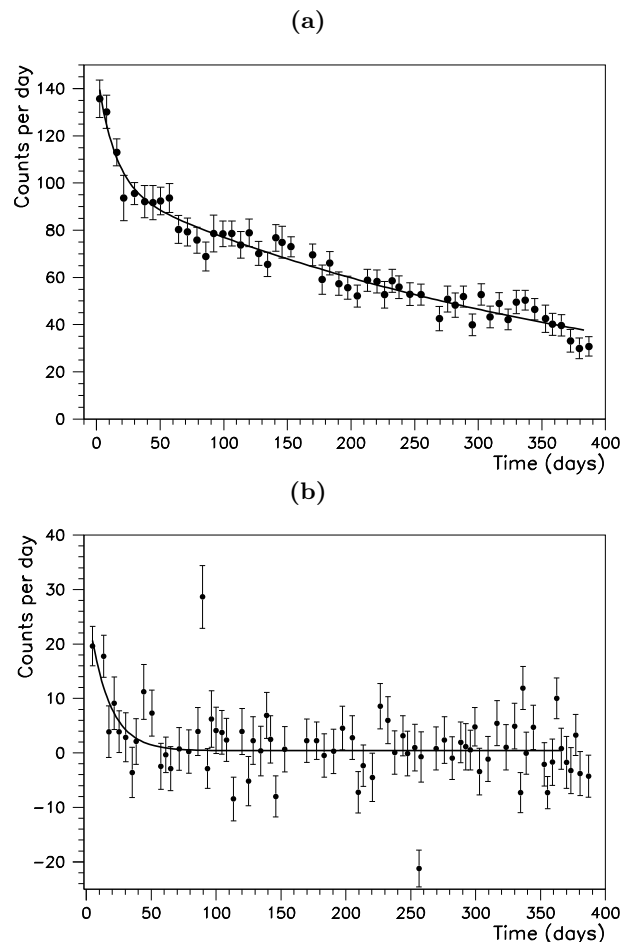
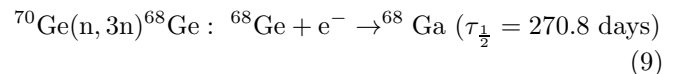
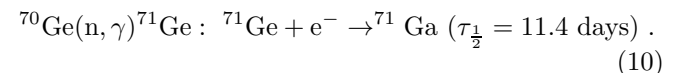


FIG. 12: The time-variation plots in Period-III data taking for γ -lines due to (a) Ga X-rays at 10.37 keV and (b) the 80.9 keV peak interpreted as γ 's from ^{133}Xe .

neutron-activated:



and



The observed exponential decays indicated that there was less neutron activation on the Ge-target inside the shield-

TABLE IV: Summary of γ -lines intensity measured in Period-III.

Energy (keV)	Isotopes	Source / Decay Series	$\tau_{\frac{1}{2}}$	Intensity ($\text{kg}^{-1}\text{day}^{-1}$)
66.7	^{73m}Ge	cosmic	0.5 s	15.4 \pm 0.4
92.6	^{234}Th	^{238}U	24.1 d	11.9 \pm 0.5
143.8	^{235}U	^{235}U	7.0 $\times 10^8$ y	5.1 \pm 0.8
185.7	^{235}U	^{235}U	7.0 $\times 10^8$ y	} 17.2 \pm 0.4
186.2	^{226}Ra	^{238}U	1600 y	
238.6	^{212}Pb	^{232}Th	10.6 h	18.8 \pm 0.5
249.8		unidentified		11.6 \pm 0.5
295.2	^{214}Pb	^{238}U	26.8 m	6.3 \pm 0.3
338.3	^{228}Ac	^{232}Th	6.2 h	3.7 \pm 0.5
351.9	^{214}Pb	^{238}U	26.8 m	17.1 \pm 0.4
463.0	^{228}Ac	^{232}Th	6.2 h	1.6 \pm 0.3
583.2	^{208}Tl	^{232}Th	3.1 m	14.4 \pm 0.3
609.3	^{214}Bi	^{238}U	19.9 m	8.1 \pm 0.2
661.7	^{137}Cs	CsI(Tl)	30.1 y	4.6 \pm 0.2
727.3	^{212}Bi	^{232}Th	66.6 m	6.4 \pm 0.2
766.4	^{234m}Pa	^{238}U	1.2 m	5.0 \pm 0.3
785.4	^{212}Bi	^{232}Th	66.6 m	} 1.7 \pm 0.4
786.0	^{214}Pb	^{238}U	26.8 m	
795.0	^{228}Ac	^{232}Th	6.2 h	2.7 \pm 0.8
834.8	^{54}Mn	reactor	312.3 d	3.6 \pm 0.3
860.6	^{208}Tl	^{232}Th	3.1 m	3.5 \pm 0.3
911.2	^{228}Ac	^{232}Th	6.2 h	19.1 \pm 0.3
964.8	^{228}Ac	^{232}Th	6.2 h	} 14.4 \pm 0.3
969.0	^{228}Ac	^{232}Th	6.2 h	
1001.0	^{234m}Pa	^{238}U	1.2 m	11.4 \pm 0.3
1120.3	^{214}Bi	^{238}U	19.9 m	6.7 \pm 0.5
1173.2	^{60}Co	reactor	5.3 y	26.0 \pm 0.3
1238.1	^{214}Bi	^{238}U	19.9 m	1.2 \pm 0.2
1332.5	^{60}Co	reactor	5.3 y	27.0 \pm 0.3
1377.7	^{214}Bi	^{238}U	19.9 m	1.9 \pm 0.3
1460.8	^{40}K	natural	1.3 $\times 10^8$ y	106.4 \pm 1.0
1509.2	^{214}Bi	^{238}U	19.9 m	0.6 \pm 0.1
1588.2	^{228}Ac	^{232}Th	6.2 h	2.5 \pm 0.1
1620.5	^{212}Bi	^{232}Th	66.6 m	1.6 \pm 0.1
1630.6	^{228}Ac	^{232}Th	6.2 h	0.6 \pm 0.1
1729.6	^{214}Bi	^{238}U	19.9 m	1.1 \pm 0.1
1764.5	^{214}Bi	^{238}U	19.9 m	5.9 \pm 0.9
1847.4	^{214}Bi	^{238}U	19.9 m	0.7 \pm 0.3
2118.6	^{214}Bi	^{238}U	19.9 m	0.2 \pm 0.1
2204.2	^{214}Bi	^{238}U	19.9 m	2.3 \pm 0.4
2447.9	^{214}Bi	^{238}U	19.9 m	0.5 \pm 0.1
2614.5	^{208}Tl	^{232}Th	3.1 m	14.5 \pm 0.2

ing structures at KS compared to the AS laboratory where the detector hardware was prepared and tested unshielded prior to installation. Coupled with these processes were the β^+ decays of ^{68}Ga ($Q=2.9$ MeV with 86% branching ratio). They were associated with two 511 keV photons emitted in coincidence, such that the ACV suppression was large.

Another interesting feature is the presence of a line at 80.9 keV observed *only once* in the beginning of the Period-III data taking, which was a Reactor OFF duration. The time evolution is displayed in Figure 12b. The

best-fit half-life of 10.6 ± 3.3 days is consistent with the interpretation of γ -emissions following β -decays of ^{133}Xe ($\tau_{\frac{1}{2}}=5.24$ days). This isotope is a fission fragment with large cumulative yield ($\sim 7\%$). It exists in gaseous form and has long enough half-life to leave the reactor core. Air pockets contaminated with ^{133}Xe might have been trapped in the vicinity of the detector during installation. Photons at this low energy were fully absorbed absorbed in the HPGe, such the time variations were confined to the peak region.

The comparisons of the key features in the measured spectra from the three periods are given in Table V. There were no hardware intervention to the shielding structures and the detectors during data taking within one period to ensure stability of the ambient conditions and of the detector operations. In between the data taking periods, there were maintenance, hardware improvement as well as detector installation efforts. The shielding door was opened and the radon purge system was temporarily disconnected. The passive shielding configurations in the inner target volume were re-assembled. All these operations were performed during Reactor ON situations to avoid the possibilities of contaminations in reactor outage. There were no incidents of sudden surge of any background during the ON-to-OFF transitions from both the HPGe detector as well as the CsI(Tl) array in all the three periods.

It can be seen from Table V that the ^{40}K activity and the before-cut background level at 30 keV associated with the experimental hardware were maintained stable during the different data taking periods. The HPGe system had a hardware failure at the end of Period-II data taking, which required the detector to be shipped back and forth by air flights to the manufacturer for repairs. Consequently, there was a sharp rise in the cosmic-induced Ga X-ray intensity between Periods II and III. The reduction in the ^{208}Tl background between Periods II and III might be due to the replacement of pre-amplifier electronic components necessary for the repairs. The background due to the ^{60}Co and ^{54}Mn contaminations at the reactor were much suppressed by the shieldings and experimental precautions, such that the detector-associated ^{40}K became the dominant γ -activity.

VII. NEUTRINO MAGNETIC MOMENTS AND RADIATIVE DECAY SEARCHES

Only the low energy spectra like the one shown in Figure 11b were used in the studies of μ_ν . Since data taking conditions were not identical among the three periods, the data were analyzed and Reactor ON/OFF spectra were compared independently within each period. Consequently, the variations in the key background features shown in Table V do not affect the evaluations of μ_ν . The analysis procedures were extended from those used previ-

TABLE V: Summary of the major spectral measurements in the three data taking periods. The intensities of the Ga X-rays are those at the start of the data taking. The others are time-averaged over an entire period.

Period	Ga X-Rays	Event Rates ($\text{kg}^{-1}\text{day}^{-1}$)				30 keV Band ($\text{kg}^{-1}\text{keV}^{-1}\text{day}^{-1}$)	
		^{40}K	^{208}Tl	^{60}Co	^{54}Mn	Before-Cut	After-Cut
I	134±6	107.2±0.7	29.2±0.3	9.8±1.0	4.2±0.7	31.6±0.1	1.58±0.02
II	45±3	106.4±0.9	25.6±0.4	14.5±1.7	3.1±0.4	31.2±0.1	1.34±0.02
III	128±7	106.4±1.0	14.5±0.2	26.5±0.2	3.6±0.3	30.9±0.1	1.42±0.01
RMS/Mean	0.40	4e-3	0.27	0.42	0.12	9e-3	0.07

ously [4] through a global treatment which incorporated additional constraints and measurements.

The PSA cut identified events with spurious and convoluted pulse shapes, some of which were due to electronic noise. These were not stable with time in general. The ACV and CRV cuts, however, rejected background due to physical processes such that the suppression factors should be stable during data taking provided that the hardware were properly controlled and cross-monitored. We denote the spectra surviving the PSA cut by ϕ_-^i and ϕ_+^i for the Reactor OFF and ON data, respectively, while those after further ACV+CRV cuts similarly by ϕ_-^f and ϕ_+^f . The before and after-cut Reactor ON spectra ϕ_+^i and ϕ_+^f in Period-III are displayed in Figure 10. The neutrino-induced contributions to the electron recoil spectra can be described by

$$\nu = \Phi_e(SM) + \kappa_e^2 \cdot \Phi_e(\mu_\nu = 10^{-10} \mu_B). \quad (11)$$

The κ_e^2 dependence on the μ_ν -signals follows from Eq. 5.

There are two constraints relating the four measured spectra within one period –

- (I) the excesses of ϕ_+^f over ϕ_-^f , if any, are neutrino-induced:

$$\phi_+^f = \epsilon \cdot \nu + \phi_-^f \quad (12)$$

where ϵ is the selection efficiency of the ACV+CRV cuts as given in Table III, and

- (II) the suppression factors for the ACV+CRV cuts should be constant between the Reactor-ON and OFF data taking:

$$\frac{\phi_+^f - \epsilon \cdot \nu}{\phi_+^i - \nu} = \frac{\phi_-^f}{\phi_-^i}. \quad (13)$$

Global minimum- χ^2 analyses were performed to the data from the three periods independently. Though the DAQ threshold was 5 keV, the analysis threshold of 12 keV was chosen to avoid complications of the atomic effects [40] as well as the time-varying background from Ga X-rays. The background profile was continuous and stable from this energy threshold up to 61 keV as expected, and could be described by a fit of a polynomial function to ϕ_-^f . The best-fit values of κ_e^2 as well as the

χ^2/dof for the three periods are listed in Table VI. It can be seen that Eqs. 12 and 13 provide excellent descriptions to the data.

TABLE VI: Summary of the best-fit results for the three periods and the χ^2/dof indicating the goodness-of-fit.

Period	Best-Fit	
	κ_e^2	χ^2/dof
I	-0.52±1.05	90/97
II	0.06±1.21	108/97
III	-0.84±0.87	84/97
Combined	-0.53±0.59	–

The data taking durations of the three periods lasted from eight to twelve months. Demonstrations of the background and detector stabilities are therefore crucial. Since each period was treated independently with its own Reactor ON and OFF data compared, the variations among the different periods shown in Table V did not lead to systematic effects on the analysis. Nevertheless, the stability (an RMS spread of 0.9%) of the before-cut levels at 30 keV among the different periods suggested that the overall background was in good control throughout the experiment.

Two complementary studies were performed on the systematic effects of the experiment, and they are discussed in details in the following paragraphs.

TABLE VII: The measured stability levels of various key spectral features, based on P-III data: R_\pm is the “residual/statistical error” ratio for the ON/OFF data, while δ_{tot} is the error/mean ratio for the entire DAQ period.

Monitors	R_\pm	δ_{tot}	χ^2/dof
^{40}K 1462 keV Band	-0.42	3.5e-3	55/53
^{208}Tl 2614 keV Band	0.18	1.3e-2	50/53
Band at 30 keV	0.005	8.2e-3	55/53
Band at 400 keV	1.3	4.1e-3	79/73
Suppression factor (ACV & CRV) at 30 keV	-0.21	9.6e-3	72/73

(1) Stability Measurements:

Several important spectral features were continuously measured to monitor and demonstrate the stabilities of the detector performance and background conditions.

These stabilities are summarized in Table VII for the 350 days of Period-III data. The monitored features included the (ACV+CRV) suppression factors, as well as the event rates of the ^{40}K and ^{208}Tl bands, together with the two sampling bands at 30 keV and 400 keV.

To quantify the stabilities, the time-evolution over the entire period was fit to a constant. The stability parameter δ_{tot} corresponds to the ratio of error/mean of the fits. The excellent values on χ^2/dof indicate that the stability hypothesis is valid and that the fluctuations of individual data points were statistical in nature. Accordingly, δ_{tot} can be taken as the stability levels of the various features being monitored. The parameter R_{\pm} denotes the ratio of residuals of Reactor ON–OFF data to their respective 1σ statistical accuracies. The measured results of $|R_{\pm}| \sim 1$ indicate that the experimental conditions were stable between the Reactor ON/OFF data set, such that their differences were consistent with statistical fluctuations, rather than due to systematic variations in hardware or background.

(2) Bounds on Possible Instabilities:

The various channels which may contribute to possible instabilities to the ON/OFF data at the low energy signal region were identified and their effects were derived from actual data and complete detector simulations. The results are summarized in Table VIIIa-c. Their effects to the ON/OFF comparisons at 30 keV, relative to the overall after-cut background $\phi(\text{cut}) \sim 1.5 \text{ kg}^{-1}\text{keV}^{-1}\text{day}^{-1}$, are denoted by δ_{\pm} .

The bounds on the ON/OFF stabilities due to event rate variations are shown in Table VIIIa. The DAQ live times were accurately measured to $\delta_{\pm} < 5\text{e-}4$ through the ratios of generated to recorded RT events. Within each period, the HPGe detector was continuously maintained at liquid nitrogen temperature to minimize the diffusion of the inactive layer which is about 1% of the active detector mass. A change of thickness of <1% implies a stability level of $\delta_{\pm} < 1\text{e-}4$.

The various background sources which may produce ON/OFF instabilities are listed in Table VIIIb, where their fractional variations are denoted by $\delta(\text{bkg})$. The evaporation rate of the liquid nitrogen in the HPGe dewar was measured to be stable to <1%. There were no observable changes [$\delta(\text{bkg}) < 5\%$] in the key spectral features in a test data set taken when this radon purge system was disconnected. Therefore, residual variations on the background due to fluctuations in radon diffusion are expected to be at the level of $\delta_{\pm} < 5\text{e-}4$.

There were five specific lines (^{54}Mn , ^{60}Co , ^{68}Ga , ^{133}Xe only for Period-III, and the 249 keV line) where variations with time were observed or should be examined. Their effects on the signal region were derived from full simulation studies using the measured peak intensities $\phi(\text{peak})$ in Table IV and $\delta(\text{bkg})$ between the ON/OFF periods as input and normalizations. The ON/OFF stabilities at the signal region are the δ_{\pm} entries in Ta-

TABLE VIII: Identified candidate channels which may contribute to Reactor ON/OFF instabilities. Their impact on Reactor ON/OFF comparisons at the 30 keV signal region (δ_{\pm}) were evaluated from P-III data and simulations. The three categories are listed separately: (a) event rate changes, (b) background variations, and (c) instabilities in detector performance and analysis efficiencies. The intrinsic stabilities of the background channels in Table (b) are given by $\delta(\text{bkg})$ while $\eta(\text{MC})$ denotes the simulated background level at the signal region with keV^{-1} bin-width, normalized to one observed event at the peak. Entries in Table (c) include the stabilities of the detector systems $\delta(\text{Detectors})$ and veto efficiencies $\delta(\text{Veto})$, while the background fraction for each mode is given by f_B . The overall uncertainty limit combined in quadratures is given in (d).

(a) Event Rate Changes				
Channels	ON/OFF Stability (δ_{\pm})			
DAQ live time	$< 5\text{e-}4$			
HPGe target mass	$< 1\text{e-}4$			
(b) Background Variations				
Background Source	ON/OFF Stability Levels			
	$\delta(\text{bkg})$	$\eta(\text{MC})$	δ_{\pm}	
Radon diffusion	< 0.05	–	$< 5\text{e-}4$	
^{54}Mn	< 0.3	$2\text{e-}3$	$< 2\text{e-}3$	
^{60}Co	< 0.06	$2\text{e-}3$	$< 4\text{e-}3$	
^{68}Ga	< 0.4	$3\text{e-}8$	$< 1\text{e-}6$	
^{133}Xe (only Period-III)	1	$4\text{e-}4$	$< 3\text{e-}3$	
Line at 249 keV	< 0.04	$1\text{e-}3$	$< 3\text{e-}4$	
(c) Detector Performance and Data Analysis				
Detector Systems & Cuts	f_B	ON/OFF Stability Levels		
		$\delta(\text{Detector})$	$\delta(\text{Veto})$	δ_{\pm}
Both CRV & ACV	0.64	$< 5\text{e-}3$	$< 1\text{e-}6$	$< 1\text{e-}5$
ACV only	0.30	< 0.05	$< 7\text{e-}4$	$< 4\text{e-}3$
CRV only	0.01	< 0.1	< 0.01	$< 2\text{e-}3$
Surviving CRV+ACV	0.05	< 0.15	–	$< 5\text{e-}4$
(d) Combined Limit				
Combined (a)+(b)+(c)				$\delta_{\pm} < 7\text{e-}3$

ble VIIIb, derived from:

$$\delta_{\pm} \sim [\phi(\text{peak}) \cdot \delta(\text{bkg}) \cdot \eta(\text{MC})] / \phi(\text{cut}) \quad (14)$$

where $\eta(\text{MC})$ is the simulated background level at the low-energy signal region with keV^{-1} bin-width, normalized to one observed event at the peak. From physical expectations, the background sources were taken to be uniformly distributed among the space in the vicinity of the HPGe detector, and their emissions were isotropic. The HPGe target was hermetically surrounded by the ACV and the detector response was mostly uniform in all directions. Consequently, the effects due to the exact source locations were small and the background levels only varied by $\sim 10\%$ (RMS) if localized point sources were used instead.

The tight limits can be understood qualitatively as follows. The weak intensity of the ^{54}Mn line and the long decay lifetime of the ^{60}Co lines suppressed the ON/OFF variations to $\delta_{\pm} < 2\text{e-}3$ and $\delta_{\pm} < 4\text{e-}3$, respectively. The decays of ^{68}Ga are mostly via the emissions of β^+ , such that the ACR was efficient as vetos in catching the two 511 keV photons. The 80.9 keV ^{133}Xe line appeared only in Period-III OFF period. At this low energy, the photoelectric cross-section is large compared to the Compton effects. The residual Compton-scattered photons were of lower energies and had large absorption by the copper cryostat as well as by the inactive layer of the HPGe. Accordingly, the effects of this line were confined to the peak region. The correlated background at the low energy signal regions were suppressed to the level of $\delta_{\pm} < 3\text{e-}3$. The short-time-scale fluctuations of the unidentified line at 249.8 keV were washed out to better than 4% when the extended ON/OFF periods were integrated, giving $\delta_{\pm} < 3\text{e-}4$.

The stabilities of the ACV and CRV detector systems, denoted by $\delta(\text{Detector})$, as well as their effects on the veto efficiencies [$\delta(\text{Veto})$] and δ_{\pm} are summarized in Table VIIIc. From Table V, the raw background rates before the ACV+CRV cuts were about $\phi(\text{raw}) \sim 30 \text{ kg}^{-1}\text{keV}^{-1}\text{day}^{-1}$ at 30 keV while the after-cut background levels were $\phi(\text{cut}) \sim 1.5 \text{ kg}^{-1}\text{keV}^{-1}\text{day}^{-1}$, such that the combined suppression factors were about 5%, as shown in Table III. The fractions of the raw background suppressed by each category of selection cuts are denoted by f_B . The ON/OFF variations at low-energy are therefore given by:

$$\delta_{\pm} \sim [f_B \cdot \delta(\text{Veto}) \cdot \phi(\text{raw})] / \phi(\text{cut}) . \quad (15)$$

About 64% of the raw background were vetoed by *BOTH* ACV and CRV. These were cosmic-ray events which penetrated the active ACV and emitted bremsstrahlung photons which interacted with the HPGe via Compton scatterings. Besides having the redundancy of signals in two detector systems, the energy depositions of these events were of the order of tens of MeV at the ACV detectors, where the threshold was about 5 keV. Consequently, the rejection efficiencies were 100% and small variations in the ACV gains or thresholds had negligible effects on the stabilities. About 30% of the raw background were tagged *ONLY* by the ACV detectors. These events were due to ambient radioactivity and typically deposited 100 keV to 1 MeV energy at the ACV. Studies were performed with both simulated and real data on the effects of the changes in software threshold. They indicated that an instability in the ACV detector gain of $\delta(\text{Detector}) \sim 5\%$ would lead only to a variation in the rejection efficiencies of $\delta(\text{Veto}) < 7\text{e-}4$, which translated to $\delta_{\pm} < 4\text{e-}3$. Similarly, only about 1% of the raw background produced CRV tag alone. These were high-energy bremsstrahlung events induced by cosmic-ray interactions with the passive shielding materials, where the

photons penetrated the ACV system. Since the PMTs of the CRV system were optimized at the stable plateau region, a 10% change in the PMT gain did not give rise to observable change in tagging efficiencies (that is, $\delta(\text{Veto}) < 1\%$), so that $\delta_{\pm} < 2\text{e-}3$. Finally, about 5% of the raw background survived both ACV+CRV cuts. The time variations of their survival probabilities were accurately measured to $\delta_{\pm} < 5\text{e-}4$ by studying the response to the same software procedures with the RT events.

TABLE IX: The various sources of the systematic uncertainties, their magnitudes $\delta(\text{Source})$ and their contributions to $\delta(\kappa_e^2)$. In particular, the first entry followed from Tables VII&VIII and is the dominant contribution.

Sources	$\delta(\text{Source})$	$\delta(\kappa_e^2)$
ON/OFF instabilities [$\delta_{\pm}(\text{combined})$]	<1%	<0.18
Efficiencies for neutrino events	<5e-4	<5e-4
Rates for $\Phi_e(\mu_{\nu})$	<3%	<0.03
$\Phi_e(\text{SM})$ background subtraction	23%	0.03
Combined Systematic Error	—	<0.18

Taking into account the measured stability levels in Table VII at the 30 keV signal region ($\delta_{\text{tot}} \sim 9\text{e-}3$), as well as the combined upper bounds on the possible Reactor ON/OFF variations ($\delta_{\pm} < 7\text{e-}3$) in Table VIII(d), an uncertainty of $\delta_{\pm}(\text{combined}) < 1\%$ was adopted to quantify the possible Reactor ON/OFF systematic instabilities at the low energy signal region. The influence of this and other sources of systematic effects are summarized in Table IX, where the stabilities of the sources are given by $\delta(\text{Source})$ while their effects on the magnetic moment searches are represented by $\delta(\kappa_e^2)$. The stabilities of the efficiencies of possible neutrino-induced signals in Table III were accurately measured to $\delta(\text{Source}) < 5\text{e-}4$ through the survival probabilities of the RT events over the various selection criteria. The $\Phi_e(\mu_{\nu})$ rates at 10-100 keV depend mostly on the *total* $\bar{\nu}_e$ flux which is well-modeled to <2% at steady-state operation [32], as discussed in details in Section IV. Residual uncertainties arise from the finite rise and fall time of the neutrino flux [26] relative to the sharp Reactor ON/OFF instants, introduced through several long-lived isotopes (like ^{93}Y , ^{97}Zr , ^{132}Te) where the total fission yield is about 15%. About 10% of the data taking time may be subjected to this effect, such that a combined uncertainty of $\delta(\text{Source}) < 3\%$ was derived for the evaluation $\Phi_e(\mu_{\nu})$. A conservative estimate of 30% systematic uncertainties for the $\phi(\bar{\nu}_e)$ spectrum below 2 MeV translates to 23% uncertainties in the $\Phi_e(\text{SM})$ background rates below 100 keV. However, this only have little impact to the accuracies in κ_e^2 since the effect being studied in $\Phi_e(\mu_{\nu})$ is an order of magnitude larger than $\Phi_e(\text{SM})$ at 10 keV.

Combining statistically the best-fit values on κ_e^2 for the three periods and adopting the systematic uncertain-

ties derived in Table IX, the results

$$\kappa_e^2 = -0.53 \pm 0.59(\text{stat.}) \pm 0.18(\text{sys.}) \quad (16)$$

were obtained. Adopting the unified approach [1], a direct limit on the $\bar{\nu}_e$ magnetic moment

$$\mu_{\bar{\nu}_e} < 7.4 \times 10^{-11} \mu_B \quad (17)$$

at 90% CL was derived. The combined residual spectrum for the three periods of the Reactor ON data over the background profiles is depicted in Figure 13. The best-fit 2σ region for κ_e^2 is superimposed. It has been verified that the correct positive signals could be reconstructed by the same analysis procedures operating on simulated spectra with μ_{ν} -induced events convoluted with similar background profiles. The results are also not sensitive to alternative choices of δ_{\pm} (combined) in Table IX given the constraints of the values in Tables VII&VIII.

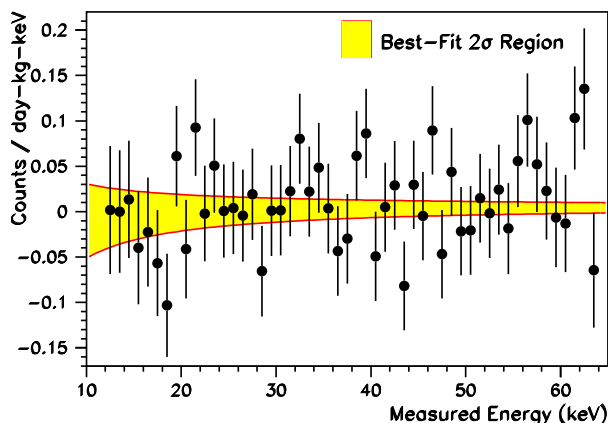


FIG. 13: The residual plot on the Reactor ON data of all periods combined over the background spectra.

Depicted in Figure 14 is the summary of the results in $\mu_{\bar{\nu}_e}$ searches versus the achieved threshold in reactor experiments. The dotted lines denote the ratios between μ_{ν} -induced and SM cross-sections [$R = \sigma(\mu)/\sigma(\text{SM})$] as functions of $(T, \mu_{\bar{\nu}_e})$. The KS(Ge) experiment has a much lower threshold of 12 keV compared to the other measurements. The large R-values imply that the KS results are robust against the uncertainties in the SM cross-sections. In particular, in the case where the excess events reported in Ref. [18] are due to unaccounted sources of neutrinos, the limits remain valid.

Results from oscillation experiments [1, 2] indicate that ν_e is predominantly a linear combination of mass eigenstates ν_1 and ν_2 with mixing angle θ_{12} given by $\sin^2\theta_{12} \sim 0.27$. The mass differences between the mass eigenstates are $\Delta m_{12}^2 \sim 8 \times 10^{-5} \text{ eV}^2$ and $\Delta m_{23}^2 \sim 2 \times 10^{-3} \text{ eV}^2$. Both “normal” (*nor*: $m_3 \gg m_2 > m_1$) and “inverted” (*inv*: $m_2 > m_1 \gg m_3$) mass hierarchies are allowed. The $\nu_1 \rightarrow \nu_3$ and $\nu_2 \rightarrow \nu_3$

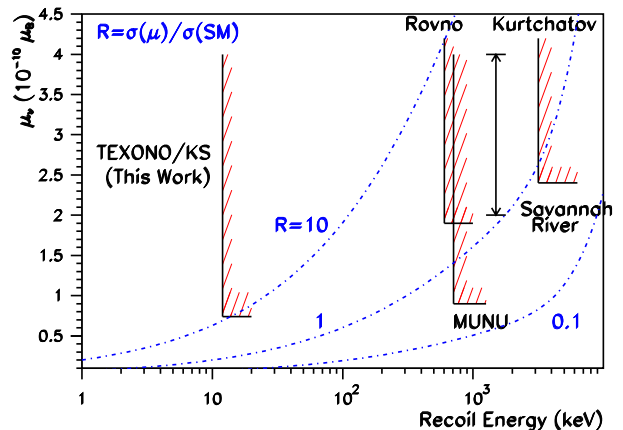


FIG. 14: Summary of the results in the searches of neutrino magnetic moments with reactor neutrinos. Both the limits and the detection thresholds of the various experiments are shown.

radiative decays are allowed only in the inverted mass hierarchy, while $\nu_2 \rightarrow \nu_1$ is possible in both hierarchies. Adopting these as input, the $\mu_{\bar{\nu}_e}$ limit of Eq. 17 can be translated via Eq. 7 to indirect bounds of

$$\frac{\tau_{13}}{m_3^3}(\text{inv} : \nu_1 \rightarrow \nu_3) > 3.2 \times 10^{27} \text{ s/eV}^3 \quad (18)$$

$$\frac{\tau_{23}}{m_2^3}(\text{inv} : \nu_2 \rightarrow \nu_3) > 1.2 \times 10^{27} \text{ s/eV}^3 \quad (19)$$

$$\frac{\tau_{21}}{m_2^3}(\text{nor} + \text{inv} : \nu_2 \rightarrow \nu_1) > 5.0 \times 10^{31} \text{ s/eV}^3 \quad (20)$$

at 90% CL. These limits are sensitive to the bare neutrino-photon couplings and are therefore valid for neutrino radiative decays in vacuum. They are summarized in Figure 15. Superimposed are the limits from the previous direct searches of excess γ 's from reactor [41] and supernova SN1987a [42] neutrinos. It can be seen that bounds inferred from ν -e scatterings are much more stringent than those of the direct approaches.

VIII. CONCLUSION AND PROSPECTS

This article describes a study of possible neutrino-photon couplings using neutrinos from nuclear power reactor as source. A germanium detector of target mass 1.06 kg was adopted as target where data taking and analysis thresholds of 5 keV and 12 keV, respectively, were achieved. Sensitive limits were derived on neutrino magnetic moments and neutrino radiative decay lifetimes. Good background level comparable to those of the underground dark matter experiments was achieved at the 10 keV range. This is the first experiment operating with such low threshold in a high neutrino flux. The unique data collected with the HPGe detector at KS open

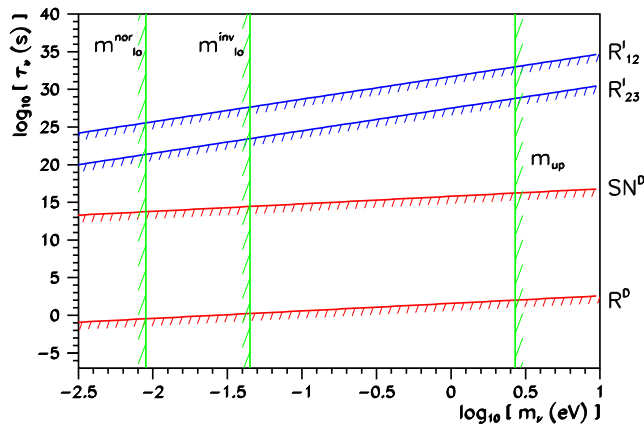


FIG. 15: Summary of the excluded parameter space on neutrino radiative decay lifetimes from $\bar{\nu}_e$ measurements. Bounds on ν_1 and ν_2 from reactor and supernova SN1987a data are denoted by R and SN, respectively. The superscripts D and I correspond to direct limits and indirect bounds inferred from magnetic moment limits, respectively. The subscript “12” is attributed to decays driven by Δm_{12}^2 , and so on. The upper bound (m_{up}) on m_ν is due to limits from direct mass measurements, while the lower bounds m_{10}^{nor} and m_{10}^{inv} are valid for the normal and inverted hierarchies, respectively. Bounds for R_{13}^I and R_{23}^I are represented by the same bands in this scale.

the possibilities of studying other phenomena like the intrinsic properties of reactor electron neutrinos [31], possible neutrino-induced nuclear transitions, and searches for reactor axions, all of which are being pursued.

The sensitivities for direct searches of neutrino magnetic moments [5] with neutrino-electron scatterings experiments scale as

$$\mu_\nu \propto \frac{1}{\sqrt{N_\nu}} \left[\frac{B}{M t} \right]^{\frac{1}{4}}, \quad (21)$$

where N_ν is the signal events at some reference magnetic moments, B , M , t are the background level, detector mass and measurement time, respectively. The best strategy to enhance the sensitivities is to have an increase on N_ν , which is proportional to the neutrino flux ϕ_ν and is related to the detection threshold. The atomic energy level effects [40], however, limit the potential sensitivity improvement as the threshold is reduced below the typical atomic scale of ~ 1 keV. There is an on-going experiment GEMMA [43] and a proposal MAMONT [44] pursuing along these directions.

However, this approach cannot improve on the μ_ν sensitivities indefinitely. Inferring from Figure 2 for reactor neutrinos, $\Phi_e(\mu_\nu)$ is only 2% of $\Phi_e(SM)$ at 1 keV as $\mu_\nu \rightarrow 10^{-12} \mu_B$. Accordingly, it would be experimentally difficult to study μ_ν by looking for anomalous effects in neutrino-electron scatterings over SM behaviour for $\mu_\nu < 10^{-12} \mu_B$. This limitation can be evaded, at least conceptually, by doing the analog of “appearance”

experiments in the case of Majorana neutrinos. One can look for signatures of anti-neutrinos of a different flavor in a pure and intense neutrino beam which passes through a dense medium or an strong magnetic field. Though there is no fundamental constraint on the lowest reach of the detectable $\bar{\nu}/\nu$ ratio, realistic accelerator-based experiments are still many orders of magnitude less sensitive than the neutrino-electron scattering experiments with reactor neutrinos [45].

The TEXONO Collaboration meanwhile is pursuing an R&D program on the “ultra-low-energy” germanium detector. A threshold of 100 eV has been achieved with a 10 g prototype [46]. The goals are to develop a ~ 1 kg detector to perform the first experimental observation of neutrino-nucleus coherent scattering using reactor neutrinos. The by-products of such an experiment will be dark matter searches at the low WIMP mass regions, as well as the probing of $\mu_{\bar{\nu}_e}$ down to the $\sim 10^{-11} \mu_B$ range.

IX. ACKNOWLEDGMENTS

The experiment reported in this article is the first particle physics experiment performed in Taiwan, as well as the first large-scale scientific collaboration among research scientists from Taiwan and China [47]. The authors are indebted to the many colleagues who have helped to “make this happen”. The invaluable contributions by the technical staff of our institutes and of the Kuo-Sheng Nuclear Power Station are gratefully acknowledged. The veto scintillator loan from the CYGNUS Collaboration is warmly appreciated. We are also grateful to the referees for comments on the treatment of systematic uncertainties. This work was supported by fundings provided by the National Science Council and the Academia Sinica, Taiwan, as well as by the National Science Foundation, China.

* Corresponding Author: htwong@phys.sinica.edu.tw; Tel:+886-2-2789-6789; FAX:+886-2-2788-9828.

- [1] See the respective sections in *Review of Particle Physics*, Particle Data Group, J. Phys. **G 33** (2006), for details and references.
- [2] See the respective articles in *Proc. of the XXIst Int. Conf. on Neutrino Phys. & Astrophys., Paris, France*, eds. J. Dumarchez, Th. Patzak, and F. Vannucci, Nucl. Phys. **B** (Proc. Suppl.) **143** (2005), for details and references.
- [3] A. de Gouvea, Nucl. Phys. **B** (Proc. Suppl.) **143**, 167 (2005).
- [4] H.B. Li et al., Phys. Rev. Lett. **90**, 131802 (2003).
- [5] H.T. Wong, Nucl. Phys. **B** (Procs. Suppl.) **143**, 205 (2005); H.T. Wong and H.B. Li, Mod. Phys. Lett. **A 20**, 1103 (2005).
- [6] B. Kayser, Phys. Rev. **D 26**, 1662 (1982); J.F. Nieves, Phys. Rev. **D 26**, 3152 (1982).

- [7] N.F. Bell et al., Phys. Rev. Lett. **95**, 151802 (2005); N.F. Bell et al., Phys. Lett. **B 642**, 377 (2006).
- [8] B.W. Lee and R.E. Shrock, Phys. Rev. **D 16**, 1444 (1977); W. Marciano and A.I. Sanda, Phys. Lett. **B 67**, 303 (1977); K. Fujikawa and R. Shrock, Phys. Rev. Lett. **45**, 963 (1980).
- [9] R. Shrock, Phys. Rev. **D 9**, 743 (1974); J. Kim, Phys. Rev. **D 14**, 3000 (1976); M.A.B. Beg, W.J. Marciano, and M. Ruderman, Phys. Rev. **D 17**, 1395 (1977); M. Fukugita and T. Yanagida, Phys. Rev. Lett. **58**, 1807 (1987); S.M. Barr, E.M. Freire, and A. Zee, Phys. Rev. Lett. **65**, 2626 (1990).
- [10] R.N. Mohapatra, S.P. Ng, and H.B. Yu, Phys. Rev. **D 70**, 057301 (2004).
- [11] J.F. Beacom and P. Vogel, Phys. Rev. Lett. **83**, 5222 (1999).
- [12] J. Schechter and J.W.F. Valle, Phys. Rev. **D 24**, 1883 (1981).
- [13] M.B. Voloshin, M.I. Vysotskii, and L.B. Okun, Sov. Phys. JETP **64**, 446 (1986); J. Barranco et al., Phys. Rev. **D 66**, 093009 (2002).
- [14] K. Eguchi et al., Phys. Rev. Lett. **90**, 021802 (2003); T. Araki et al., Phys. Rev. Lett. **94**, 081801 (2005).
- [15] A.B. Balantekin and C. Volpe, Phys. Rev. **D 72**, 033008 (2005).
- [16] D.W. Liu et al., Phys. Rev. Lett. **93**, 021802 (2004).
- [17] G.G. Raffelt, “Stars as Laboratories for Fundamental Physics”, Sect. 7.5, U. Chicago Press (1996).
- [18] P. Vogel and J. Engel, Phys. Rev. **D 39**, 3378 (1989).
- [19] P.P. Pal and L. Wolfenstein, Phys. Rev. **D 25**, 766 (1982).
- [20] G.G. Raffelt, Phys. Rev. **D 39**, 2066 (1989).
- [21] F. Reines, H.S. Gurr, and H.W. Sobel, Phys. Rev. Lett. **37**, 315 (1976).
- [22] G.S. Vidyakin et al., JETP Lett. **55**, 206 (1992).
- [23] A.I. Derbin et al., JETP Lett. **57**, 769 (1993).
- [24] C. Amsler et al., Nucl. Instrum. Methods **A 396**, 115 (1997); Z. Daraktchieva et al., Phys. Lett. **B 615**, 153 (2005).
- [25] W. Grimus et al., Nucl. Phys. **B 648**, 376 (2003); M.A. Tortola, hep-ph/0401135 (2004).
- [26] H.B. Li and H.T. Wong, J. Phys. **G 28**, 1453 (2002).
- [27] FISCOF Ver 1.0, W.S. Tong, 08-4-MAN-036-001-1.1, Institute of Nuclear Energy Research (2001); FISS-RATE Ver 2.0, W.S. Kuo, 08-4-MAN-036-002-1.0, Institute of Nuclear Energy Research (2001).
- [28] CASMO-3 Ver 4.84, Malte Edenius et al., STUDSVIK/SOA-94/9, Studsvik Scandpower (1994); SIMULATE-3 Ver 6.07.08, Lorne Covington et al., STUDSVIK/SOA-95/15 Rev. 2, Studsvik Scandpower (2001).
- [29] P. Vogel et al., Phys. Rev. **C 24**, 1543 (1981).
- [30] V.I. Kopeikin, L.A. Mikaelyan, and V.V. Sinev, Phys. Atom. Nucl. **60**, 172 (1997).
- [31] B. Xin et al., Phys. Rev. **D 72**, 012006 (2005).
- [32] Y. Declais et al., Phys. Lett. **B 338**, 383 (1994).
- [33] B. Achkar et al., Phys. Lett. **B 374**, 243 (1996).
- [34] H.T. Wong, Mod. Phys. Lett. **A 19**, 1207 (2004).
- [35] H.B. Li et al., Nucl. Instrum. Methods **A 459**, 93 (2001).
- [36] W.P. Lai et al., Nucl. Instrum. Methods **A 465**, 550 (2001).
- [37] ULB-HPGe Model GC5019, Canberra Industries, USA.
- [38] VME-PCI Adaptor, Model 618, SBS Technologies, USA.
- [39] Redundant Array of Independent Disks (RAID), Ultra Trak SX8000, Promise Technology, USA.
- [40] V.I. Kopeikin et al., Phys. Atom. Nucl. **60**, 2032 (1997).
- [41] L. Oberauer, F. von Feilitzsch, and R.L. Mössbauer, Phys. Lett. **B 198**, 113 (1987); J. Bouchez et al., Phys. Lett. **B 207**, 217 (1988).
- [42] E.L. Chupp, W.T. Vestrand, and C. Reppin, Phys. Rev. Lett. **62**, 505 (1989).
- [43] A.G. Beda et al., Phys. Atom. Nucl. **67**, 1948 (2004).
- [44] L.N. Bogdanova, Nucl. Phys. **A 721**, 499 (2003)
- [45] M.C. Gonzalez-Garcia, F. Vannucci, and J. Castromonte, Phys. Lett. **B 373**, 153 (1996); J.-M. Frère, R.B. Nevzorov, and M.I. Vysotsky, Phys. Lett. **B 394**, 127 (1977).
- [46] H.T. Wong, J. Phys. Conf. Ser. **39**, 266 (2006).
- [47] D. Normile, Science **300**, 1074 (2003).

